Effect of calcination temperatures on microstructures and photocatalytic activity of tungsten trioxide hollow microspheres

Jiaguo Yu*, Lifang Qi, Bei Cheng, Xiufeng Zhao

State Key Laboratory of Advanced Technology for Material Synthesis and processing, Wuhan University of Technology, Luoshi Road 122, Wuhan 430070, PR China

ABSTRACT

Tungsten trioxide hollow microspheres were prepared by immersing $SrWO_4$ microspheres in a concentrated HNO_3 solution, and then calcined at different temperatures. The prepared tungsten oxide samples were characterized by X–ray diffraction, X–ray photoelectron spectroscopy, Fourier transform infrared spectra, differential thermal analysis–thermogravimetry, UV–visible spectrophotometry, scanning electron microscopy, N_2 adsorption/desorption measurements. The photocatalytic activity of the samples was evaluated by photocatalytic decolorization of rhodamine B aqueous solution under visible-light irradiation. It was found that with increasing calcination temperatures, the average crystallite size and average pore size increased, on the contrary, Brunauer–Emmett–Teller-specific surface areas decreased. However, pore volume and porosity increased firstly, and then decreased. Increasing calcination temperatures resulted in the changes of surface morphology of hollow microspheres. The un-calcined and 300 °C-calcined samples showed higher photocatalytic activity than other samples. At 400 °C, the photocatalytic activity decreased greatly due to the decrease of specific surface areas. At 500 °C, the photocatalytic activity of the samples increased again due to the junction effect of two phases.

1. Introduction

Oxide semiconductor photocatalysis has been extensively investigated since Fujishima and Honda discovered the photocatalytic splitting of water on TiO_2 electrodes in 1972 [1]. Compared with conventional oxidation processes, oxide semiconductor photocatalysis has several obvious advantages including complete mineralization of the pollutants, application of the near-UV or solar light, no addition of other chemicals, operation at near room temperature, low cost, and so forth [2–7]. Recently, fabrication of various micrometer- and nanometer-sized oxide hollow sphere photocatalysts have attracted considerable attention because of their low density, high surface area, good surface permeability as well as hollow textures [8–14]. It is expected that high photocatalytic activity and large adsorption efficiencies could be achieved using oxide hollow spheres as photocatalysts. Up to now, the most important methods for the preparation of hollow structures rely on the use of sacrificial templates, either hard or soft template, and the desired hollow interiors are generated upon the removal of templates by calcination or dissolution [15]. Very recently, we have developed a novel one-pot template-free synthesis method for the preparation of various hollow structures based on direct solid evacuation via chemically induced self-transformation method [10–12].

Tungsten oxide is widely used in electrochromic windows, infrared switching devices, photocatalysis, writing–reading erasing optical devices, and gas sensors for detecting NO_2, H_2S, NH_3, H_2, O_3, and H_2O [16–18]. Li et al. had reported the fabrication of nanometer-sized WO_3 hollow spheres via the hydrolysis of WCl_6 using pre-synthesized carbon microspheres as templates [19]. We also reported the preparation of micrometer-sized WO_3 hollow spheres using the as-prepared $SrWO_4$ spheres as precursors [16]. However, there are few reports on photocatalytic activity of WO_3 hollow microspheres. In this work, we investigated the effect of calcination temperatures on the microstructures and photocatalytic activity of WO_3 hollow microspheres.

2. Materials and methods

2.1. Materials

All the chemicals used in this study were in analytical grade and from Shanghai Chemical Regent Factory of China except polymethacrylic acid (PMAA), which was from Sigma–Aldrich, without further purification. Distilled water was used in all experiments.

2.2. Sample preparation

The detailed experimental process for the preparation of $SrWO_4$ can be found in our previous studies [16]. Three starting aqueous solutions, $SrCl_2$ (0.1 mol/L), Na_2WO_4 (0.1 mol/L) and PMAA

(10 g/L) were prepared firstly. In a typical experiment, 10 mL of SrCl$_2$ solution (0.1 mol/L), 0.5 mL of PMAA solution (10 g/L) and 29.5 mL of distilled water were mixed in a baker under magnetic stirring for 5 min. Then, 10 mL of Na$_2$WO$_4$ solution (0.1 mol/L) was slowly added under vigorous stirring, giving final concentrations of 0.02 mol/L for both Sr^{2+} and WO$_4^{2-}$, and 0.1 g/L for PMAA. The starting pH value of the mixture was adjusted to 12 using 2 mol/L NaOH and HCl solutions. After continuous vigorous stirring for 5 min, the mixture was sealed and incubated at room temperature for 12 h. The resulting white precipitate was collected, washed with distilled water and ethanol, and dried in air. Tungsten oxide hydrate hollow microspheres were obtained by soaking the as-prepared SrWO$_4$ samples in a concentrated HNO$_3$ solution (8 mol/L) at room temperature for 24 h, and then washed with distilled water and ethanol for three times, respectively. The washed precipitates were dried in a vacuum oven at 60 °C for 8 h and finally were calcined at 300, 400, 500, 600 and 700 °C for 2 h in air, respectively.

2.3. Characterization

X-ray diffraction (XRD) patterns obtained on an X-ray diffractometer (type HZG41B–PC) using Cu Kα irradiation at a scan rate of 0.05° 2θ s^{-1} were used to determine the identity of crystalline phase present and their crystallite size. The accelerating voltage and applied current were 15 kV and 20 mA, respectively. X-ray photoelectron spectroscopy (XPS) measurements were done with a VG ESCALAB 210 with Mg Kα source and a charge neutralizer; all the binding energies were referenced to the C1s peak at 284.8 eV of the surface adventitious carbon. The Brunauer–Emmett–Teller (BET) surface area (S_{BET}) of the powders was analyzed by nitrogen adsorption in a Micromeritics ASAP 2020 nitrogen adsorption apparatus (USA). All samples calcined were degassed at 180 °C prior to nitrogen adsorption measurements, while the sample without calcination was degassed at 100 °C. BET surface area was determined by a multipoint BET method using the adsorption data in the relative pressure (P/P_0) range of 0.05–0.3. Desorption isotherm was used to determine the pore-size distribution via a Barret–Joyner–Halender (BJH) method, assuming a cylindrical pore modal [20,21]. The nitrogen adsorption volume at the relative pressure (P/P_0) of 0.974 was used to determine the pore volume and average pore size. The morphologies of all samples were observed by a JSM-5610LV scanning electron microscope (SEM) at an acceleration voltage of 20 kV and a S4800 Field Emission SEM (FESEM, Hitachi, Japan) at an accelerating voltage of 5 kV and linked with an Oxford Instruments X-ray analysis system. UV–vis spectra of all samples were taken on an UV–visible spectrophotometer (UV-2550, Japan). BaSO$_4$ was used as a reflectance standard in the UV–vis diffuse reflectance experiment. The differential thermal analysis–thermogravimetry (DTA–TG) was performed using a TG-DTA instrument (Setaram TG-DTA 92-16, France), under an air flow of 100 mL/min at a heating rate of 10 °C/min from room temperature to 1000 °C. Infrared absorption spectra were recorded for KBr disks containing the sample using an FTIR spectrometer (Nialet–60SXB, American).

2.4. Measurement of photocatalytic activity

Dyes are important industrial pollutants. Most dyes are resistant to biodegradation and direct photolysis, and many N-containing dyes such as rhodamine B (RhB) undergo natural reductive anaerobic degradation to yield potentially carcinogenic aromatic amines [22]. Therefore, we chose RhB as a model contamination to evaluate the photocatalytic activity of tungsten trioxide samples. The photocatalytic activity evaluation of tungsten trioxide samples for the photocatalytic decolorization of RhB aqueous solution was per-
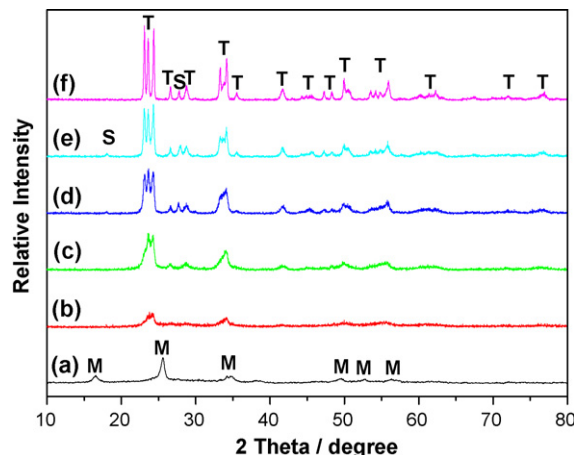

Fig. 1. XRD patterns of the samples before (a) and after calcinations at 300 (b), 400 (c), 500 (d), 600 (e) and 700 °C (f) for 2 h. T: WO$_3$, S: SrWO$_4$ and M: WO$_3$·H$_2$O.

formed at ambient temperature in air. Experiments were as follows: The catalysts were prepared by coating an aqueous suspension of WO$_3$ powders onto three dishes with a diameter of about 9.0 cm. The weight of catalysts used in each experiment was kept 0.02 g. The dishes containing catalysts were dried in an oven at 80 °C for about 4 h to evaporate the water and then cooled to room temperature before used. 20 mL of RhB aqueous solution with a concentration of 1.0×10^{-5} mol/L was added into the dishes coated with catalysts in each experiment. An 18 W daylight lamp was used as a light source. Prior to irradiation, the dishes containing catalysts and RhB were kept in dark for 2 h to reach the adsorption/desorption equilibrium between catalysts and RhB molecules. After visible-light irradiation for some time, the reaction solution was filtrated to measure the concentration change of RhB by recording the changes of the intensity of absorption peak at 554 nm using an UV–visible spectrophotometer (UV-2550, Shimadzu, Japan). According to the Lambert–Beer Law [23], the absorbance (A) of RhB is proportional to its concentration (c), which generally followed the following equation:

$$A = \varepsilon bc \qquad (1)$$

where ε is the molar absorption coefficient and b is the thickness of the absorption cell. In our experiment, all the testing parameters were kept constant, so the ε and b can be considered as fixed value. Therefore, the concentration of RhB aqueous solution can be expressed by A. As for the RhB aqueous solution with low concentration, its photocatalytic decolorization is a pseudo-first-order reaction and its kinetics may be expressed as follows [24]:

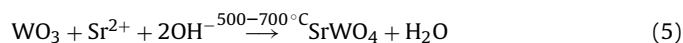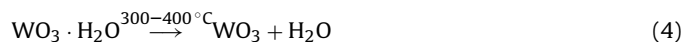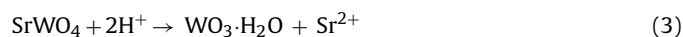$$\ln \left(\frac{A_0}{A_t} \right) = kt \qquad (2)$$

where k is the apparent rate constant, and A_0 and A_t are the initial and reaction absorbance of RhB aqueous solution, respectively.

3. Results and discussions

3.1. Phase structure

XRD was used to investigate the changes of phase structures of the as-prepared samples before and after calcinations. Fig. 1 shows effects of calcination temperatures on phase structures of the samples. Before calcinations, all diffraction peaks of the sample can be indexed to a pure orthorhombic WO$_3$·H$_2$O (JCPDS card no. 84-0886, $a = 5.249$ Å, $b = 10.711$ Å, $c = 5.133$ Å). At 300 and 400 °C, all diffraction peaks can be indexed to a pure monoclinic WO$_3$ (JCPDS card

no. 72-1465, $a = 7.3$ Å, $b = 7.53$ Å, $c = 7.68$ Å), indicating the removal of structure water of $WO_3 \cdot H_2O$ and occurrence of phase transformation from $WO_3 \cdot H_2O$ to WO_3. When calcination temperatures are above 500 °C, it can be easily found from Fig. 1 that besides the diffraction peaks of monoclinic WO_3, two new peaks at 2θ about 18.0° and 27.7° are observed, which can be indexed to tetragonal $SrWO_4$ (JCPDS card no. 89–2568, $a = 5.4$ Å, $b = 11.91$ Å). Why do the samples contain a small amount of $SrWO_4$ at high temperatures? One possible explanation is that Sr^{2+} ions are not completely removed during washing. This can be well understood in terms of viewpoint of isoelectric point. The isoelectric point of WO_3 is very low and about 0.5 [25]. Hence, when pH values of the reaction system exceed 0.5, the surface of WO_3 particles will be negatively charged and would be expected to experience a significant electrostatic attraction to positive Sr^{2+} ions. Thus, Sr^{2+} ions will deposit on the surface or interior of WO_3 microspheres due to the electrostatic attraction between Sr^{2+} ions and WO_3. It is not surprising that the adsorbed Sr^{2+} ions are hard to be completely removed via washing, and they would coexist with WO_3 microspheres. Therefore, it is not difficult to understand the formation of $SrWO_4$ at high temperature due to solid phase reaction between Sr^{2+} ions and WO_3. The following XPS results also further confirm the above explanation. Further observation indicate that the peak intensities of monoclinic WO_3 increase, the peak profiles become more and more sharp and narrow, implying that the enhancement of crystallization and the growth of WO_3 crystallite size (see Table 1). Main reactions involved are summarized as follows:

$$SrWO_4 + 2H^+ \rightarrow WO_3 \cdot H_2O + Sr^{2+} \tag{3}$$

$$WO_3 \cdot H_2O \overset{300-400\,°C}{\longrightarrow} WO_3 + H_2O \tag{4}$$

$$WO_3 + Sr^{2+} + 2OH^- \overset{500-700\,°C}{\longrightarrow} SrWO_4 + H_2O \tag{5}$$

3.2. SEM studies

SEM was used to investigate the influence of calcination temperatures on the morphologies of hollow microspheres. Fig. 2 shows SEM images of the samples before and after calcination. All the samples appear obviously hollow nature and calcination temperatures have no obvious influence on the size of WO_3 hollow microspheres (diameter ranges from 3.0 to 5.5 µm). The thicknesses of hollow spheres are determined by observing cross-section of broken spheres and are about 300–500 nm. The rugged surface suggests that the hollow spheres are composed of small crystallites. With increasing calcination temperatures, the roughness of the particles increases. At 300 and 400 °C, the shells are composed of flake-like nanoparticles with a thickness of about 50 nm. At 500 °C, the thickness of flake-like nanoparticles increases. At 700 °C, the sizes of nanoparticles on the shells increase drastically and reach about 300–500 nm. The spheres become much looser (see Fig. 2e) and porous surface structures formed due to loose aggregation between large crystallites. These morphology changes are caused by phase transformation and restructures of particles

and growth of crystallites. This observation is in agreement with the grain size calculation based on the Debye–Scherrer formula (as shown Table 1).

3.3. FT–IR spectroscopy

FT–IR spectra of samples before and after calcination are shown in Fig. 3. All the samples show a strong absorption at 600–1000 cm^{-1}, which is associated with the W—O—W stretching mode [26,27]. The weak bands at 1010–1040 cm^{-1} are attributed to the stretching of W=O bonds at the surface [27]. The bands at 1631 cm^{-1} are assigned to the H—O—H bending vibrations of water, which are easily introduced into the system during the IR measurements. Samples calcined at different temperatures exhibit different profiles in the absorption region between 600 and 1000 cm^{-1}. The un-calcined sample shows corner-sharing vibration of W—O_b and terminal vibration of W—O_d at 669 and 950 cm^{-1}, respectively, indicating that the structure of $WO_3 \cdot H_2O$ [28–30] is composed of basic units of WO_6 octahedra linked by shared corners, like in WO_3 [30–32], but in a more open framework. For the sample calcined, the peak at 950 cm^{-1} becomes weaker and weaker and the main absorption peaks at 669 cm^{-1} shift to the region of higher wave number, splitting into two peaks at 754 and 815 cm^{-1}, respectively. Although variation of the temperature causes no much change in the position of these two peaks, it makes their intensity change obviously. When the temperature is below 500 °C, the peak at 754 cm^{-1} associated with edge-sharing vibration of W—O_c is stronger than the other peak at 815 cm^{-1} associated with bridging vibration of W—O—W, while it is just opposite when the temperature is above 500 °C. At 500 °C, they have nearly the same intensity. With increasing temperature, the main absorption bands become narrower, indicating the growth of grains (shown in Table 1).

3.4. Thermal analysis

Fig. 4 shows DTA–TG curves of the dried sample. The endothermic peak at 126 °C is due to the evaporation of the physically adsorbed water and ethanol solvent. The small endothermic peak at 231 °C can be ascribed to the evaporation of crystal water. The exothermic peak at about 317 °C is probably caused by the phase transformation of the sample from orthorhombic ($WO_3 \cdot H_2O$) to monoclinic (WO_3) (see Fig. 1). A relative small endothermic peak at 370 °C may be caused by the loss of a small amount of structure water. The exothermic peak at 508 °C comes from two causes: one is the enhancement of crystallization of WO_3; the other is the formation of new phase $SrWO_4$. There is another endothermic peak at 608 °C, which can be ascribed to the decomposition of $SrWO_4$. Therefore, the peak intensities of $SrWO_4$ decrease when the calcination temperature increases to 700 °C. The widest exothermic peak at 880 °C comes from the phase transformation of the monoclinic (γ) to tetragonal (α) phase of WO_3 [33,34].

The TG curve can be roughly divided into three stages. The largest weight loss (8.51%) is observed from room temperature to 230 °C, this can be attributed to the evaporation of the physically

Table 1
Effects of calcination temperatures on physical properties of the tungsten trioxide hollow microspheres

Temperature (°C)	Phase structures[a]	S_{BET} (m^2/g)	Pore volume (cm^3/g)	Average pore size (nm)	Porosity (%)	Crystalline size (nm)
No calcination	M	36.2	0.054	6.0	23.6	14
300	T	31.1	0.070	9.0	33.7	16
400	T	18.9	0.071	15.1	34.3	16
500	T,S	4.5	0.018	15.7	12.8	17
600	T,S	1.3	0.005	16.8	3.77	27
700	T,S	0.7	–	–	–	47

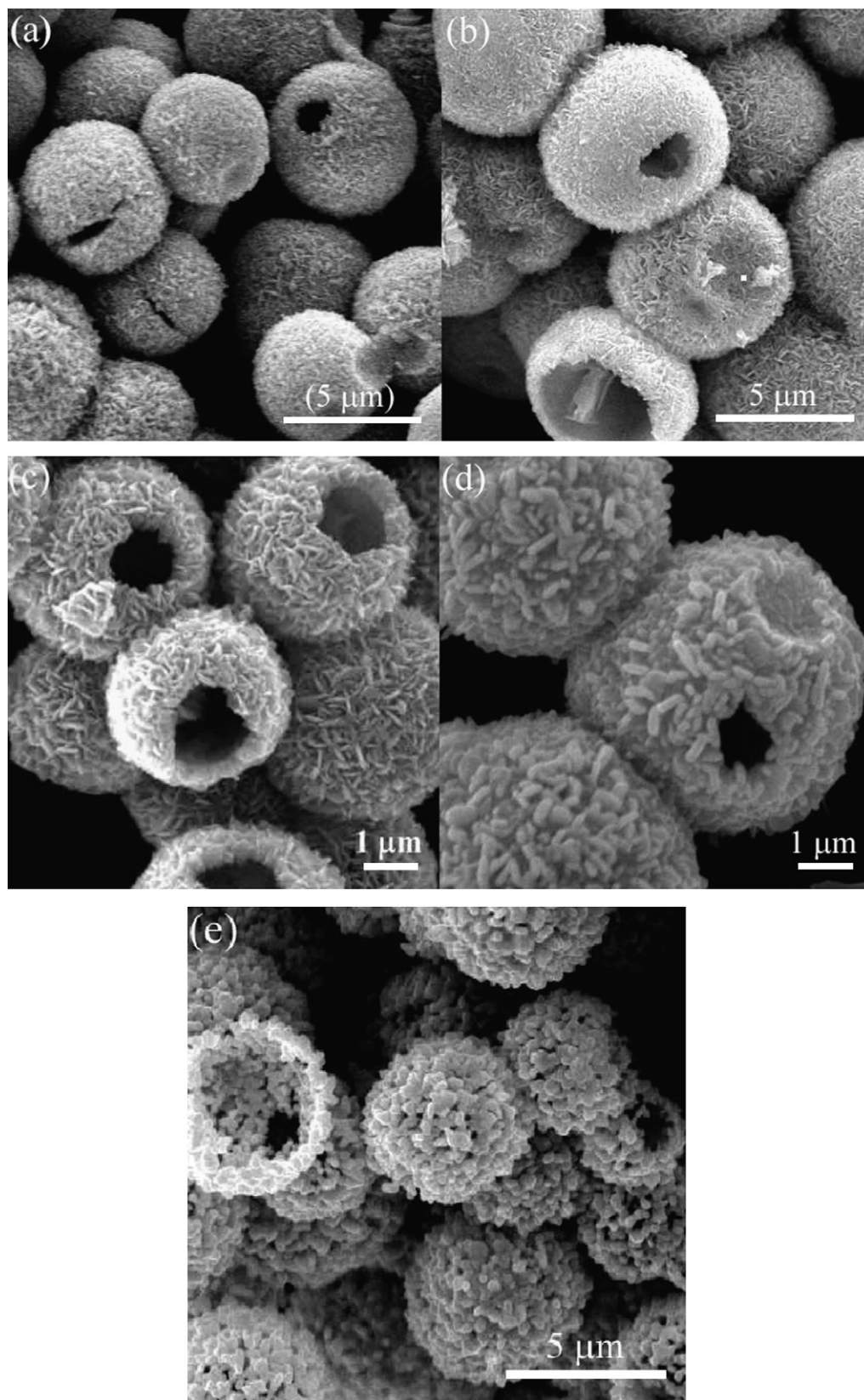[a] M, T and S denote $WO_3 \cdot H_2O$, WO_3 and $SrWO_4$, respectively.

Fig. 2. SEM images of the samples before (a) and after calcinations at 300 (b), 400 (c), 500 (d) and 700 °C (e) for 2 h.
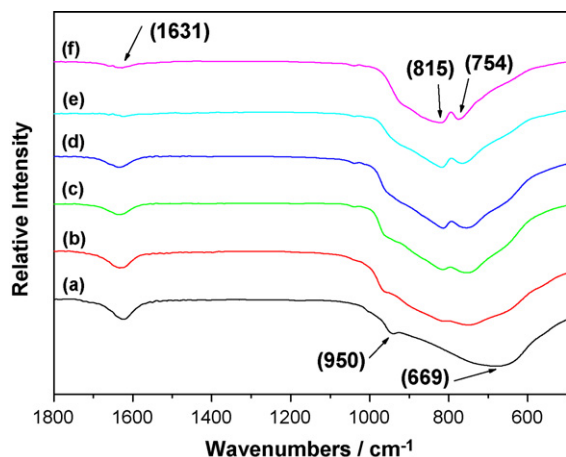
Fig. 3. FTIR spectra of the samples before (a) and after calcinations at 300 (b), 400 (c), 500 (d), 600 (e) and 700 °C (f) for 2 h.
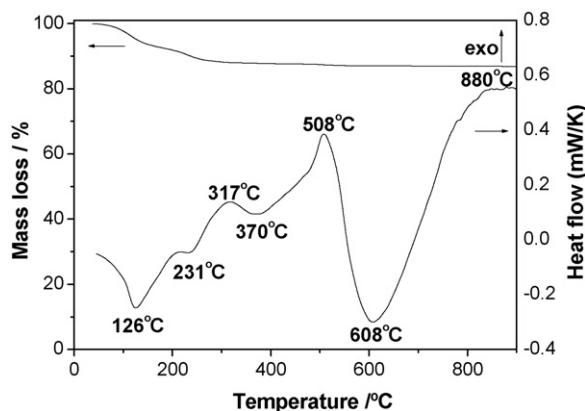

Fig. 4. DTA–TG curves of the un-calcined sample.

Fig. 5. XPS survey spectra of the un-calcined (a) and 500 °C-calcined samples (b).

adsorbed water, some crystallization water and other chemicals. The second stage is from 230 to 317 °C, and the mass loss is 3.27%. This can be assigned to the evaporation of the residual crystallization water. The third stage is from 317 to 1000 °C, a mass loss of about 1.37% is due to the dehydration and evaporation of chemisorbed water.

3.5. XPS studies

Fig. 5 shows XPS survey spectra of the samples before and after calcinations at 500 °C. The XPS spectra of the two samples are similar, containing not only W and O elements, but also a small amount of Sr and C elements. The XPS peak for C1s at $E_b = 284.8$ eV is due to the adventitious hydrocarbon from the XPS instrument itself. The XPS peak for Sr observed in the spectra is due to the residual elements from precursor $SrWO_4$, implying that Sr^{2+} ions are not completely removed by water washing. Fig. 6A shows the high-resolution XPS spectra of the Sr 3d region for the samples before and after calcinations. Calcination at 500 °C causes the shift of position of Sr 3d peaks to a lower binding energy region, suggesting the changes of chemical status of Sr^{2+} ions from adsorbed status to chemical status ($SrWO_4$) and formation of $SrWO_4$ due to high solid phase reaction between Sr^{2+} and WO_3. This is consistent with the XRD results. The high-resolution XPS spectra of the O 1s region are shown in Fig. 6B. Before calcinations, the O 1s region of the sample can be fitted into two peaks. One is ascribed to O—H groups (binding energy at 533.0 eV), associated with the chemisorbed (or
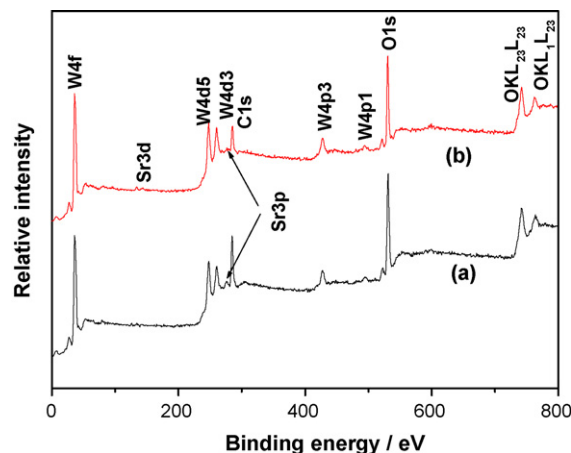
crystallization) H_2O. Although some H_2O is physically adsorbed on the surface of the sample, the physisorbed H_2O is easily desorbed under the ultra-high vacuum condition of the XPS system [35,36]. So there is no peak of physisorbed H_2O observed in the XPS spectra. The other is attributed to W—O bond (binding energy at 530.9 eV). At 500 °C, the peak of O—H disappeared, indicating the loss of crystallization water and the change of phase structures from $WO_3 \cdot H_2O$ to WO_3 and $SrWO_4$. This is also in good agreement with XRD results (see Fig. 1). Moreover, the position of W—O peak also shifts to a lower binding energy region. The XPS spectra of W 4f region for the samples before and after calcinations are shown in Fig. 6C. The spectra show a well-resolved doublet due to the tungsten $4f_{7/2}$ and $4f_{5/2}$ components observed at binding energies of 35.8 and 37.9 eV, respectively. Their highly symmetry indicates that the samples contain only W^{6+} state. Also, the position of the doublet for the sample calcined at 500 °C shifts to a lower binding energy region, also indicating the change of chemical environment of W^{6+}.

3.6. BET surface areas and pore distributions

Figs. 7 and 8 show the nitrogen adsorption/desorption isotherms of the samples before and after calcinations and their corresponding pore-size distributions, respectively. The isotherm corresponding to the un-calcined sample is of type IV (BDDT classification) with two capillary condensation steps, implying the bimodal pore-size distributions in the mesoporous and macroporous region. The hysteresis loop in lower relative pressure range ($0.4 < P/P_0 < 0.8$) is related to finer intra-aggregated pore within the agglomerated particles, and that in higher relative pressure range ($0.8 < P/P_0 < 1$) is associated with larger inter-aggregated pore between the aggregated particles [37,38]. This bimodal mesopore size distribution is confirmed by the corresponding pore-size distributions (see Fig. 8). The powders contain small mesopores (peak pore at 3.7 nm) and larger mesopores with a peak pore diameter of *ca.* 39.1 nm. Calcination temperatures obviously influence the pore structures and BET surface areas of the samples. With increasing calcination temperatures, the isotherms corresponding to the samples obtained at 300 and 400 °C show higher absorption at high relative pressure (P/P_0) range (approaching 1), indicating the formation of more macropores and/or the increase of pore volume (see Table 1). Further observation indicates that the hysteresis loop in low relative pressure range gradually disappears and the two separate hysteresis loops gradually join together as one, suggesting that the pore-size distributions of intra-aggregated pores and inter-aggregated ones tend to overlap, as confirmed in Fig. 8. This is associated with the growth of the crystallites, phase trans-
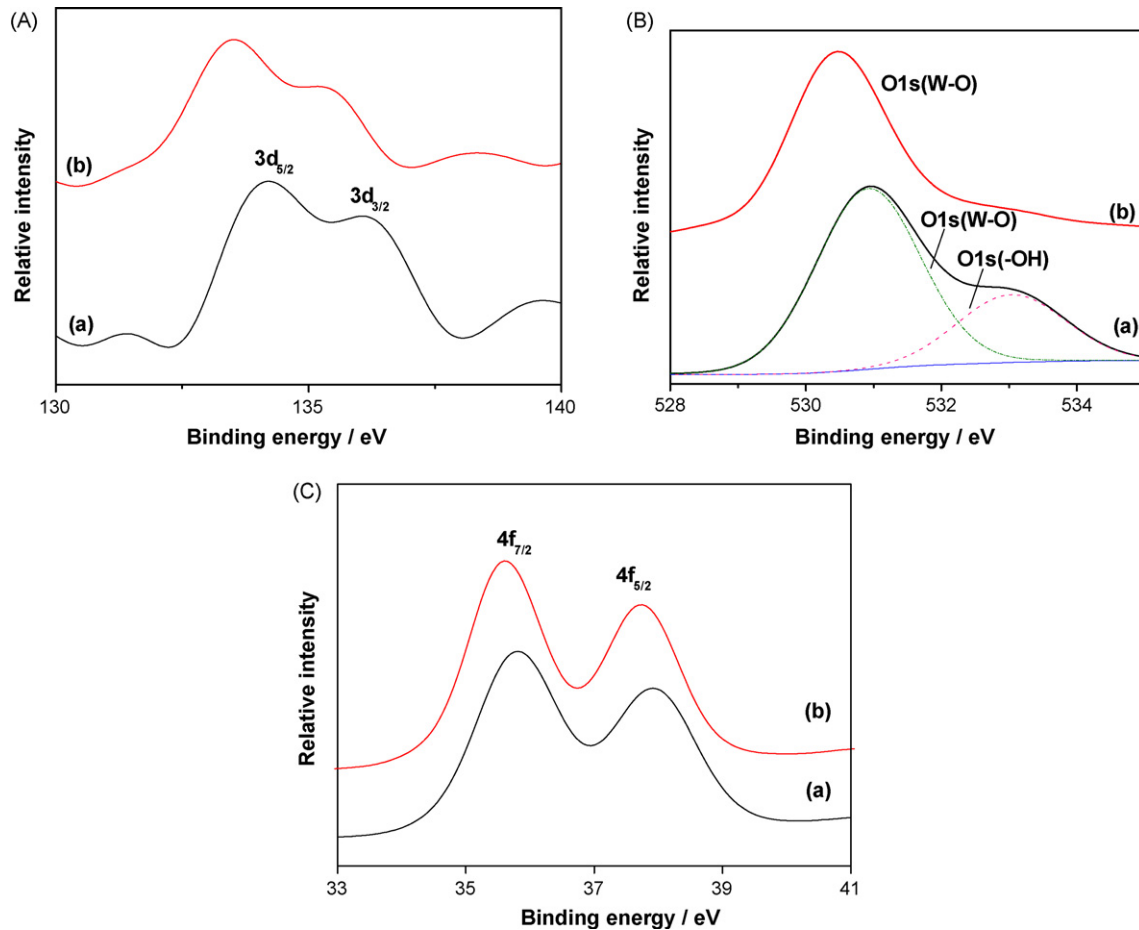
Fig. 6. High-resolution XPS spectra of Sr 3d (A), O 1s (B) and W 4f (C) regions of the un-calcined (a) and 500 °C-calcined samples (b).

formation and re-structures of particles and the shrinkage of the aggregates, resulting in the right-shift of intra-aggregated pores and left-shift of inter-aggregated ones, respectively. When calcination temperatures are above 500 °C, the hysteresis loop in low relative pressure range completely disappears and the areas of hysteresis loop decrease greatly, implying the decrease of pore volume (see Table 1) and the collapse of intra-aggregated pores, which is confirmed by the corresponding monomodal pore distribution (Fig. 8).
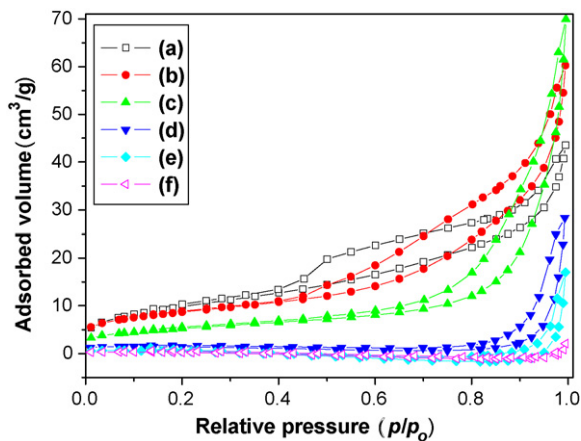
3.7. UV–vis diffuse reflectance spectra

Fig. 9 displays the UV–vis diffuse reflectance spectra of the samples before and after calcinations. A significant increase at the absorption wavelengths shorter than 500 nm can be assigned to the intrinsic bandgap absorption of tungsten trioxide due to the electron transitions from the valence band to conduction band ($O_{2p} \rightarrow W_{5d}$). With increasing calcination temperatures, the samples show an obvious change in the absorption edges, indicating
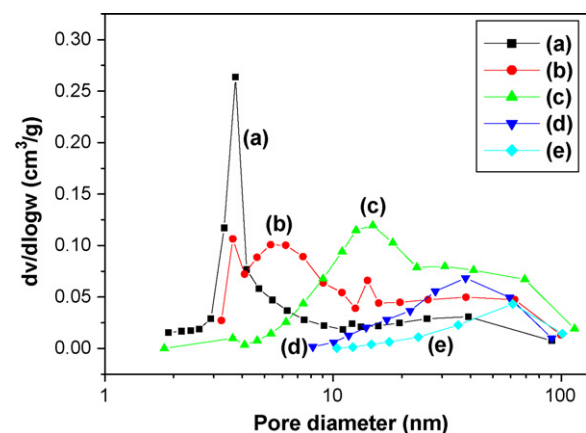

Fig. 7. Nitrogen adsorption/desorption isotherms of the samples before (a) and after calcinations at 300 (b), 400 (c), 500 (d), 600 (e) and 700 °C (f) for 2 h.

Fig. 8. Pore-size distribution curves of the samples before (a) and after calcinations at 300 (b), 400 (c), 500 (d) and 600 (e) for 2 h.
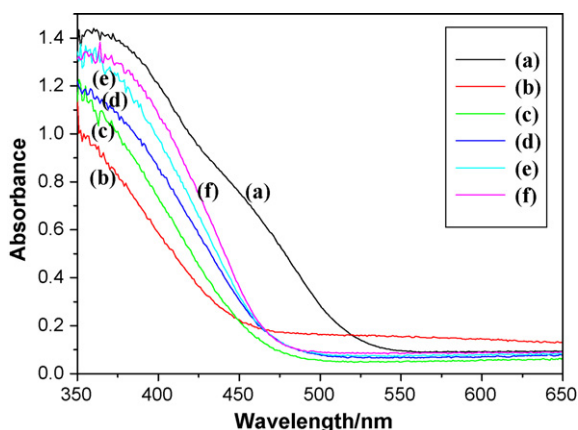
Fig. 9. UV–vis absorption spectra of the samples before (a) and after calcinations at 300 (b), 400 (c), 500 (d), 600 (e) and 700 °C (f) for 2 h.

Fig. 10. Comparison of the apparent rate constants of the samples before (a) and after calcinations at 300 (b), 400 (c), 500 (d), 600 (e) and 700 °C (f) for 2 h.

the difference of bandgap energy. Plot of $(\alpha h\nu)^2$ versus photon energy $(h\nu)$ will give a good approximation of the bandgap energy for a crystalline semiconductor (not shown here) [39]. The bandgap energies estimated from the intercept of the tangents to the plots are about 2.30, 2.70, 2.63, 2.60, 2.58 and 2.57 eV for the samples before and after calcinations at 300, 400, 500, 600 and 700 °C, respectively. The un-calcined sample shows a smallest bandgap energy among all samples, because it has the different composition ($WO_3 \cdot H_2O$) and crystal structure (orthorhombic system). After calcinations, all the samples show obvious blue shift, implying the increase of bandgap energies due to the changes of phase structures. At 300 °C, the bandgap of sample WO_3 is 2.70 eV, which is agreement with literature value [17–19]. With further increasing calcination temperatures, the bandgap energies slightly decrease probably due to the incorporation of the Sr species into the WO_3 structure or formation of $SrWO_4$.

3.8. Photocatalytic activity

The visible-light photocatalytic activity of the samples was evaluated by photocatalytic decolorization of RhB aqueous solution. However, under dark conditions without visible-light illumination, the concentration of RhB has no obvious change for every measurement using various tungsten trioxide samples. Illumination in the absence of tungsten trioxide samples does not result in the photocatalytic decolorization of RhB. Therefore, the presence of both illumination and tungsten trioxide samples is necessary for the efficient photocatalytic degradation. These results also suggest that the degradation decolorization of RhB aqueous solution is caused by photocatalytic reactions on tungsten trioxide samples under the visible-light illumination [24].

Fig. 10 shows the effects of calcination temperatures on the photocatalytic activity of the samples. It can be seen that the un-calcined and 300 °C-calcined samples show higher photocatalytic activity than other samples. This can be ascribed to their relative large surface areas and small crystallite size (see Table 1) [40–43]. At 400 °C, the photocatalytic activity decreases greatly. This can be well understood according to the decrease of specific surface areas. However, at 500 °C, the photocatalytic activity of the samples increases again. Why does the 500 °C sample have a higher photocatalytic activity than the 400 °C sample? One possible explanation is that the 500 °C sample contains WO_3 and $SrWO_4$ two phases. Usually, the composite of two kinds of semiconductors or two phases of the same semiconductor is beneficial in reducing the combination of photogenerated electrons and holes and enhancing photocatalytic activity [36,38,39]. Furthermore, the decrease
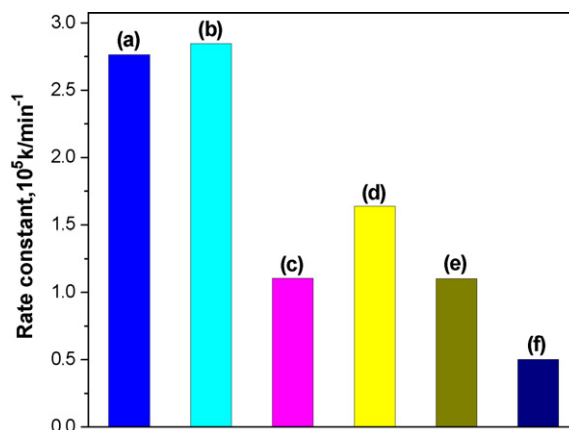
of photocatalytic activities of the samples at above 500 °C might be explained by the decrease of specific surface areas and pore volume, the increase of crystallite size and sintering of crystallites [40–43]. Of course, the detailed photocatalytic degradation mechanism of RhB using tungsten trioxide as photocatalyst under visible-light irradiation need to be further carefully investigated.

Our experimental results also show that tungsten trioxide hollow spheres can be more readily separated from the slurry system by filtration or sedimentation after photocatalytic reaction and re-used than conventional powder photocatalytic materials. Therefore, the prepared tungsten trioxide hollow spheres can be regarded as a good photocatalyst for environmental purification at industrial scale. To the best of our knowledge, this is the first time to report the photocatalytic activity of nanoporous tungsten trioxide hollow spheres calcined at different temperatures. We believe that the prepared tungsten trioxide hollow spheres are also of great interest in solar cell, catalysis, separation technology, biomedical engineering and nanotechnology [42,43].

4. Summary

(1) The un-calcined hollow spheres appear bimodal pore-size distribution and contain small mesopores (peak pore at 3.7 nm) and larger mesopores (peak pore size: *ca.* 39.1 nm). With increasing calcination temperatures, the hysteresis loop in low relative pressure range gradually disappears and the two separate hysteresis loops gradually join together as one. When calcination temperatures are above 500 °C, the samples appear monomodal pore distribution.

(2) Calcination temperatures also show obvious influence on the surface morphology and microstructures of the hollow microspheres. With increasing calcination temperatures, the average crystallite size and average pore size increased, on the contrary, BET-specific surface areas decreased. However, pore volume and porosity increased firstly, and then decreased. Increasing calcination temperature resulted in the changes of surface morphology of hollow microspheres.

(3) The un-calcined and 300 °C-calcined samples show higher photocatalytic activity than other samples. At 400 °C, the photocatalytic activity decreases greatly due to the decrease of specific surface areas of the samples. At 500 °C, the photocatalytic activity of the samples increases again due to the junction effect of two phases. The hollow microsphere samples can be more readily separated from the slurry system after photocatalytic reaction.

Acknowledgements

References

[1] A. Fujishima, K. Honda, Electrochemical photolysis of water at a semiconductor electrode, Nature 238 (1972) 37.

[2] M.R. Hoffmann, S.T. Martin, W.Y. Choi, D.W. Bahnemann, Environmental applications of semiconductor photocatalysis, Chem. Rev. 95 (1995) 69.

[3] P.V. Kamat, R. Huehn, R. Nicolaescu, A "sense and shoot" approach for photocatalytic degradation of organic contaminants in water, J. Phys. Chem. B 106 (2002) 788.

[4] J.G. Yu, Y.R. Su, B. Cheng, Template-free fabrication and enhanced photocatalytic activity of hierarchical macro-/mesoporous titania, Adv. Funct. Mater. 17 (2007) 1984.

[5] J.G. Yu, L.J. Zhang, B. Cheng, Y.R. Su, Hydrothermal preparation and photocatalytic activity of hierarchically sponge-like macro-/mesoporous titania, J. Phys. Chem. C 111 (2007) 10582.

[6] J.G. Yu, X.J. Zhao, Q.N. Zhao, Effect of surface structure on photocatalytic activity of TiO_2 thin films prepared by sol–gel method, Thin Solid Films 379 (2000) 7.

[7] F.B. Li, X.Z. Li, M.F. Hou, Photocatalytic degradation of 2-mercaptobenzothiazole in aqueous La^{3+}–TiO_2 suspension for odor control, Appl. Catal. B 48 (2004) 185.

[8] A. Syoufian, O.H. Satriya, K. Nakashima, Photocatalytic activity of titania hollow spheres: photodecomposition of methylene blue as a target molecule, Catal. Commun. 8 (2007) 755.

[9] X.F. Song, L. Gao, Fabrication of hollow hybrid microspheres coated with silica/titania via sol–gel process and enhanced photocatalytic activities, J. Phys. Chem. C 111 (2007) 8180.

[10] H.G. Yu, J.G. Yu, S.W. Liu, S. Mann, Template-free hydrothermal synthesis of CuO/Cu_2O composite hollow microspheres, Chem. Mater. 19 (2007) 4327.

[11] J.G. Yu, S.W. Liu, H.G. Yu, Microstructures and photoactivity of mesoporous anatase hollow microspheres fabricated by fluoride-mediated self-transformation, J. Catal. 249 (2007) 59.

[12] J.G. Yu, H.T. Guo, S.A. Davis, S. Mann, Fabrication of hollow inorganic microspheres by chemically induced self-transformation, Adv. Funct. Mater. 16 (2006) 2035.

[13] H. Li, Z. Bian, J. Zhu, D. Zhang, G. Li, Y. Huo, H. Li, Y. Lu, Mesoporous titania spheres with tunable chamber structure and enhanced photocatalytic activity, J. Am. Chem. Soc. 129 (2007) 8406.

[14] H.G. Yu, J.G. Yu, B. Cheng, S.W. Liu, Novel preparation and photocatalytic activity of one-dimensional TiO_2 hollow structures, Nanotechnology 18 (2007) 065604.

[15] F. Caruso, Hollow capsule processing through colloidal templating and self-assembly, Chem. Eur. J. 6 (2000) 413.

[16] X. Zhao, T.L.Y. Cheung, X. Zhang, D.H.L. Ng, J. Yu, Facile preparation of strontium tungstate and tungsten trioxide hollow spheres, J. Am. Ceram. Soc. 89 (2006) 2960.

[17] K. Bange, T. Gambke, Electrochromic materials for optical switching devices, Adv. Mater. 2 (1990) 10.

[18] M.D. Antonik, J.E. Schneider, E.L. Wittman, K. Snow, J.F. Vetelino, Microstructural effects in WO_3 gas-sensing films, Thin Solid Films 256 (1995) 247.

[19] X.L. Li, T.J. Lou, X.M. Sun, Y.D. Li, Highly sensitive WO_3 hollow-sphere gas sensors, Inorg. Chem. 43 (2004) 5442.

[20] K.S.W. Sing, D.H. Everett, R.A.W. Haul, L. Moscou, R.A. Pierotti, J. Rouquerol, T. Siemieniewska, Reporting physisorption data for gas/solid systems with special reference to the determination of surface area and porosity, Pure Appl. Chem. 57 (1985) 603.

[21] E.P. Barrett, L.G. Joyner, P.H. Halenda, The determination of pore volume and area distributions in porous substances. I. Computations from nitrogen isotherms, J. Am. Chem. Soc. 73 (1951) 373.

[22] H. Fu, C. Pan, W. Yao, Y. Zhu, Visible-light-induced degradation of rhodamine B by nanosized Bi_2WO_6, J. Phys. Chem. B 109 (2005) 22432.

[23] H. Kumazawa, M. Inoue, T. Kasuya, Photocatalytic degradation of volatile and nonvolatile organic compounds on titanium dioxide particles using fluidized beds, Ind. Eng. Chem. Res. 42 (2003) 3237.

[24] J.G. Yu, H.G. Yu, B. Cheng, X.J. Zhao, J.C. Yu, W.K. Ho, The effect of calcination temperature on the surface microstructure and photocatalytic activity of TiO_2 thin films prepared by liquid phase deposition, J. Phys. Chem. B 107 (2003) 13871.

[25] A.P. George, The isoelectric points of solid oxides, solid hydroxides, and aqueous hydroxo complex systems, Chem. Rev. 65 (1965) 177.

[26] G. Ramis, C. Cristiani, A.S. Elmi, P. Villa, Characterization of the surface properties of polycrystalline WO_3, J. Mol. Catal. 61 (1990) 319.

[27] C.G. Barraclough, J. Stals, Spectral and structural studies of some Group VIA dioxydihalides, Aust. J. Chem. 19 (1966) 741.

[28] M.L. Freedman, The tungstic acids, J. Am. Chem. Soc. 81 (1959) 3834.

[29] B. Gerand, G. Nowogrocki, J. Guenot, M. Figlarz, A new tungsten trioxide hydrate, $WO_3 \cdot \frac{1}{3}H_2O$: preparation, characterization, and crystallographic study, J. Solid State Chem. 38 (1981) 312.

[30] R. Nedjar, M.M. Borel, M. Hervieu, B. Raveau, Une nouvelle forme de trioxyde de tungstene: Les oxydes WO_3 et $WO_3 \cdot O,5H_2O$ a structure pyrochlore, Mater. Res. Bull. 23 (1988) 91.

[31] S. Tanisaki, Crystal structure of monoclinic tungsten trioxide at room temperature, J. Phys. Soc. Jpn. 15 (1960) 573.

[32] B. Gerand, G. Nowogrocki, J. Guenot, M. Figlarz, Structural study of a new hexagonal form of tungsten trioxide, J. Solid State Chem. 29 (1979) 429.

[33] T. Vogt, P.M. Woodward, P.A. Hunter, The high-temperature phases of WO_3, J. Solid State Chem. 144 (1999) 209.

[34] E. Cazzanelli, C. Vinegoni, G. Mariotto, A. Kuzmin, J. Purans, Low-temperature polymorphism in tungsten trioxide powders and its dependence on mechanical treatments, J. Solid State Chem. 143 (1999) 24.

[35] J.G. Yu, J.C. Yu, W.K. Ho, Z.T. Jiang, Effects of calcination temperature on the photocatalytic activity and photo-induced super-hydrophilicity of mesoporous TiO_2 thin films, New J. Chem. 26 (2002) 607.

[36] J.G. Yu, J.F. Xiong, B. Cheng, S.W. Liu, Fabrication and characterization of Ag–TiO_2 multiphase nanocomposite thin films with enhanced photocatalytic activity, Appl. Catal. B 60 (2005) 211.

[37] J.G. Yu, G.H. Wang, B. Cheng, M.H. Zhou, Effects of hydrothermal temperature and time on the photocatalytic activity and microstructures of bimodal mesoporous TiO_2 powders, Appl. Catal. B 69 (2007) 171.

[38] J.G. Yu, J.C. Yu, M.K.P. Leung, W.K. Ho, B. Cheng, X.J. Zhao, Effects of acidic and basic hydrolysis catalysts on the photocatalytic activity and microstructures of bimodal mesoporous titania, J. Catal. 217 (2003) 69.

[39] J.C. Yu, J.G. Yu, W.K. Ho, Z.T. Jiang, L.Z. Zhang, Effects of F^- doping on the photocatalytic activity and microstructures of nanocrystalline TiO_2 powders, Chem. Mater. 14 (2002) 3808.

[40] X.Z. Li, F.B. Li, C.L. Yang, W.K. Ge, Photocatalytic activity of WO_x–TiO_2 under visible light irradiation, J. Photochem. Photobiol. A 141 (2001) 209.

[41] F.B. Li, X.Z. Li, M.F. Hou, K.W. Cheah, W.C.H. Choy, Enhanced photocatalytic activity of Ce^{3+}–TiO_2 for 2-mercaptobenzothiazole degradation in aqueous suspension for odour control, Appl. Catal. A 285 (2005) 181.

[42] J.G. Yu, H.G. Yu, H.T. Guo, M. Li, S. Mann, Spontaneous formation of a tungsten trioxide sphere-in-shell superstructure by chemically induced self-transformation, Small 4 (2008) 87.

[43] J.G. Yu, S.W. Liu, M.H. Zhou, Enhanced photocalytic activity of hollow anatase microspheres by Sn^{4+} incorporation, J. Phys. Chem. C 112 (2008) 2050.